

Ultra-precise optical to radio frequency based chip-scale refractive index and temperature sensor

LIRON STERN, ALEX NAIMAN, GAL KEINAN, NOA MAZURSKI, MEIR GRAJOWER, AND URIEL LEVY*

Department of Applied Physics, The Benin School of Engineering and Computer Science, The Center for Nanoscience and Nanotechnology, The Hebrew University of Jerusalem, Jerusalem 91904, Israel

*Corresponding author: ulevy@mail.huji.ac.il

Received 2 August 2016; revised 3 November 2016; accepted 15 November 2016 (Doc. ID 272956); published 21 December 2016

Chip-scale high-precision measurements of physical quantities such as temperature, pressure, refractive index, and analytes have become common with nanophotonics and nanoplasmonics resonance cavities. Despite several important accomplishments, such optical sensors are still limited in their performances in the short and, in particular, long time regimes. Two major limitations are environmental fluctuations, which are imprinted on the measured signal, and the lack of miniaturized, scalable robust and precise methods of measuring optical frequencies directly. Here, by utilizing a frequency-locked loop combined with a reference resonator, we overcome these limitations and convert the measured signal from the optical domain to the radio-frequency domain. By doing so, we realize a highly precise on-chip sensing device with sensing precision approaching 10^{-8} in effective refractive index units, and 90 μK in temperature. Such an approach paves the way for single particle detection and high-precision chip-scale thermometry. © 2016 Optical Society of America

OCIS codes: (130.6010) Sensors; (230.5750) Resonators; (060.5625) Radio frequency photonics; (120.6780) Temperature.

<https://doi.org/10.1364/OPTICA.4.000001>

1. INTRODUCTION

Resonance cavities are excellent transducers to convert small variations in the local refractive index into measurable spectral shifts. As such, these cavities are being used extensively in a variety of disciplines ranging from, e.g., bio-sensing [1–5], chemical sensing [6], temperature sensing [7], and pressure gauges [8–10] to atomic and molecular spectroscopy [11]. Specifically, chip-scale microring and microdisk resonators (MRRs) are widely used for these purposes [12–14] owing to their miniaturized size, relative ease of design and fabrication, high quality factor, and versatility in the optimization of their transfer function.

The principle of operation of such resonative sensors is based on monitoring the wavelength dependence of the resonator subject to minute variation in its surrounding (e.g., different types of atoms and molecules, gases, pressure, temperature). Traditionally, wavelength monitoring has been achieved either by comparing the spectra prior to and after the sensing event, or by monitoring the resonator's temporal intensity variations at a fixed frequency. Yet both techniques are akin to thermal drifts and other noise sources of both the MRR and the interrogating laser, which limit the sensitivity and accuracy of such measurements both in the long and the short terms. Thus, in order to monitor such minute perturbations to the refractive index over time (representing, for example, the temporal changes in a concentration of a molecule), one needs to have both the MRR and the laser fully stabilized. The level of such stabilization will dictate the sensitivity limit of the system. Considering a silicon photonic chip operating

as a refractive index sensor, with a target refractive index sensitivity of 10^{-8} , which is beyond the current state of the art, one needs to stabilize the MRR to the $\sim 100 \mu\text{K}$ regime, while the laser needs to be stabilized to the megahertz level. Stabilization to such values is highly challenging. In order to overcome frequency uncertainties and enable real-time and precise sensing, it is desired to implement a differential sensing scheme. Indeed, such schemes have been explored using either external reference systems or more recently by the use of a reference MRR on-chip [14,15].

While the concept of a reference resonator provides a significant advance, the implementation of highly precise sensing is still limited to the quality of the local oscillator, e.g., the laser that is being used and the ability to precisely define the resonance frequency by using conventional spectroscopic measurements. A promising approach for overcoming these bottlenecks is the implementation of active frequency stabilization schemes. Frequency modulation (FM) spectroscopy, wavelength modulation (WM), and the similar Pound–Drever–Hall techniques are widely used to lock the radio and optical frequencies to a desired resonance frequency and to measure the dispersive properties of resonant phenomena [16–18]. In these methods, a signal proportional to frequency difference of the local oscillator and the resonator (coined an error signal) is fed back to the local oscillator, and consequently aligns the laser to the desired resonance. Indeed, by using such schemes the stabilization of different sources has been made possible [19,20]. Moreover, one can simultaneously monitor the resonator frequency variations with high precision

[21]. Indeed, it should be noted that the precision of such frequency variations can substantially exceed the Q -factor. For example, in an atomic clock a frequency uncertainty ($\Delta f/f$) of 10^{-11} at time constant of 1 s is achieved [22], being often 5 orders of magnitude smaller than the inverse Q -factor of the atomic line.

Here, taking advantage of concepts borrowed from the well-established field of frequency metrology, and exploiting the differential immunity of our cascaded MRR system to environmental perturbations, we demonstrate a sensing platform enabling both short and long time highly precise sensing. Specifically, we frequency lock two independent lasers to two MRRs, which are situated in the vicinity of each other on the same chip. As the frequency difference between the MRRs is in the radio-frequency (RF) regime, our system has the capability to transduce minute environmental perturbations, (e.g., in the form of pressure variations, temperature variations, or the presence of analyte and particles) to a RF signal. By doing so, and considering the ability to measure RFs exceptionally precisely, a conceptual breakthrough in nanophotonics-based sensing is achieved. To demonstrate the usefulness of our approach, we measure the difference between these two frequency locked lasers by beating them upon a photodetector, achieving a highly sensitive sensor capable of measuring a refractive index uncertainty of $1.5 \cdot 10^{-7}$ RIU $\cdot \tau^{-1/2}$ (τ being the averaging time constant), with an unprecedented noise floor of $1.5 \cdot 10^{-8}$ RIU, equivalent to temperature uncertainty of about 90 μ K at ~ 200 s. Typical drifts were measured to be 10^{-7} RIU/h enabling long time stability in the state-of-the-art level and even beyond. One direct application of our system is the measurement of local temperatures and temperature gradients on a chip. This latter issue is becoming in the modern era, when the local heating of central processing units (CPUs) is becoming one of the major bottlenecks preventing the improvement of computer performance beyond the current state of the art. Having a CMOS compatible platform that can perform such precise temperature measurements without being sensitive to electromagnetic noise is greatly needed. We cope with this issue by inducing a temperature gradient between the two MRRs. By doing so, we are able to distinctly demonstrate an on-chip local thermometer capable of measuring temperature differences as low as 0.8 mK over the course of minutes, corresponding to a measurement uncertainty of $1.2 \text{ mK} \cdot \tau^{-1/2}$.

2. EXPERIMENTAL RESULTS

A. Fabrication and Concept of Operation

A schematic representation of our differential sensing apparatus is sketched in Fig. 1(a), where we present a chip consisting of two

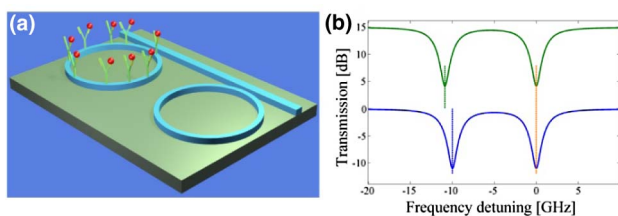


Fig. 1. (a) Schematic representation of cascaded MRRs. (b) Illustration of the spectrum of the reference MRR (in blue) and the sensing MRR (solid green and dashed green). The sensing MRR curve is illustrated with and without the refractive index change.

cascaded MRRs coupled to a bus waveguide. The first (right MRR) serves as the reference MRR, while the second (left MRR) is the sensing unit, which is subject to the perturbation to be measured (analytes, temperature, pressure, etc.). We seek to monitor the refractive index variations of this sensing MRR, which manifest as a resonance frequency shift, as illustrated in Fig. 1(b). Here, two adjacent resonance lines (green line) originating from each of the cascaded MRRs are illustrated. The frequency difference between these two lines is 10 GHz, and is assumed to be relatively constant, as both MRRs are subject to the same environment. By applying a perturbation to the sensing MRR, this frequency difference will change, as illustrated in the blue line in Fig. 1(b). Thus, monitoring the frequency difference yields a precise and accurate method to measure small changes in refractive index, temperature, or pressure. Moreover, as the ability to accurately (orders of magnitude better than what is reported in this paper) measure RFs is readily available, relatively cheap, and miniaturized, the proposed method offers a prominent advantage with respect to optical differential schemes.

In Fig. 2(a) we present a scanning electron micrograph (SEM) of the two cascaded MRRs. The MRR chips presented here are fabricated using low-loss waveguides based on the concept of local oxidization of silicon (LOCOS) [23–26]. The waveguide dimensions were 450 nm width and 220 nm height, whereas the MRR radius was 30 μ m. Next, we characterize the transmission spectrum of the cascaded MRRs. In Fig. 2(b), we plot the transmission of the MRRs as a function of wavelength. We observe a few distinct absorption dips separated by the free spectral range (FSR) of the MRR (corresponding to ~ 3 nm). By closely examining the spectrum [Fig. 3(c)], we observe that each dip within an FSR consists of two distinct dips, with a separation of 78.5 pm corresponding to 10.03 GHz. Such frequency separation complies with the abovementioned requirement for an easily detectable separation in the RF regime. Finally, the resonance of each dip is ~ 30 pm wide, corresponding to a Q -factor of about 50,000, with extinction of about 15 dB.

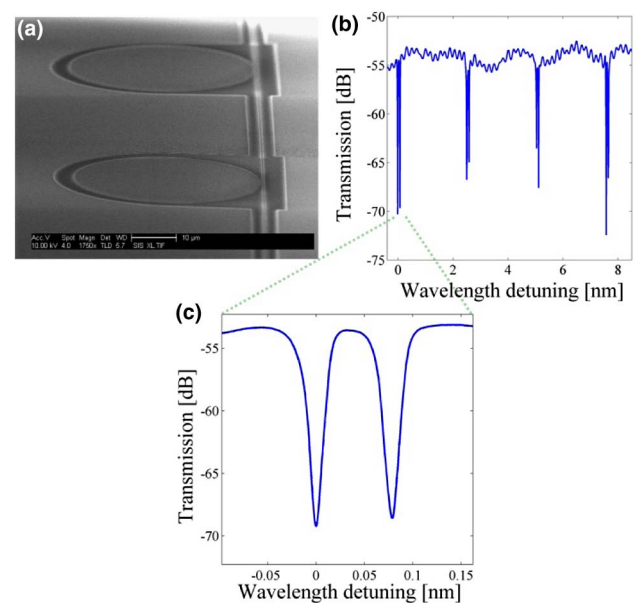


Fig. 2. (a) SEM image of the cascaded LOCOS MRRs. (b) Measured spectrum of the cascaded MRRs. (c) Zoomed transmission around two adjacent dips, separated by 78.5 pm/10.03 GHz.

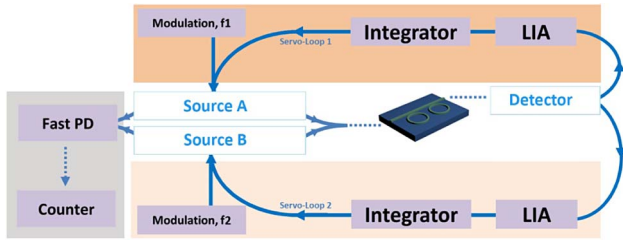


Fig. 3. Schematic illustration of dual locking schemes. Two lasers are locked simultaneously to the cascaded MRRs. The beat signal of these two lasers is measured using an oscilloscope or a spectrum analyzer.

Next, in Fig. 3 we illustrate a schematic representation of the dual locking scheme. Each locking scheme relies on the acquisition of a signal proportional to the difference between the laser frequency and the MRR frequency. This error signal is fed back to the laser's frequency actuator. Specifically, two lasers, labeled "source A" and "source B," are combined and coupled to our cascaded MRR chip. Both lasers are wavelength modulated by two different frequencies, f_1 and f_2 , being in the few 100 Hz regime, and with a modulation depth corresponding to a fraction of the width of the resonators. The signal of both lasers is coupled through the bus waveguide to a lensed fiber connected to an InGaAs detector. The generated photocurrent feeds two lock-in amplifiers (LIAs), referenced to two different frequencies, f_1 and f_2 . The demodulated signals provide us with error signals that are redirected to sources A and B. Such error signals, which can be viewed as the differential of the MRR lineshape, provide the laser with the needed "correction" in order to be aligned with the MRR. An additional integrator serves as a "memory" for each individual servo-loop. Such technique is well established, and more details and implementations can be found in, for instance, Refs. [27–30]. Finally, to monitor the frequency difference between the two MRRs, sources A and B are combined to illuminate a fast photodetector. The frequency beat signal is monitored using a RF frequency counter.

Finally, we add an electrical switch connected to the output of the modulation f_1 and f_2 . We do so because using wavelength modulation, i.e., operating at low frequencies and relatively high modulation depths, yields a dithered beat spectrum. Obviously such a spectra is difficult to interpret. By switching the modulation (and "freezing" the integrator's output), we are able to obtain clear beat signals. In future implementations, this switching can be avoided using either frequency modulation [16], where the modulation frequency has to exceed the resonators width, or the previously demonstrated dither cancellation techniques [28].

B. Frequency-Locked Loop Results

Next, we apply the locking scheme presented earlier, and characterize the system capabilities. To do so, we tune both lasers to the vicinity of the resonance dips and close the two servo-loops. Now, the two lasers frequencies are aligned with two adjacent resonant frequencies, each originating from a different MRR. To verify that indeed the difference in resonance frequencies between the two MRRs is relatively stable over time, we monitor both integrators' outputs (representing the error signals) as a function of time. In Fig. 4(b) we plot typical error signals of both MRRs.

One can clearly observe that the two error signals follow each other, thus the lasers are tracking each MRR individually in a

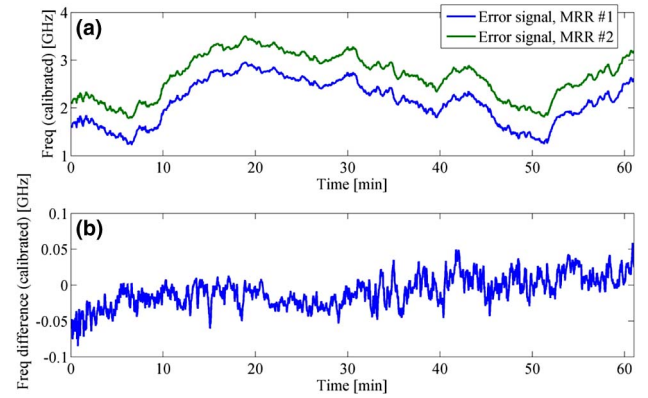


Fig. 4. (a) Calibrated integrators output as a function of time of both servo-loops. (b) Difference between the integrators output as function of time.

correlated fashion. We attribute this correlation in error signal to be mainly due to temperature fluctuations in the room. Such temperature fluctuations affect both MRRs almost identically, as both MRRs are subjected to a very similar heat environment: they are situated on the same chip, in close vicinity to each other, and are of the same dimensions and materials. Using the thermo-optic coefficient of silicon [31] ($1.8 \cdot 10^{-4}$ RIU/K), and by calibrating the frequency modulation transfer function of the lasers, we estimate room temperature fluctuations of about 0.1°K , which is a typical value measured in our laboratory over a time scale of 1 h. Finally, in Fig. 4(b), we plot the error signal difference. It can be readily seen that the error signal difference deviations are much smaller than the deviations of each of the error signals. The deviations of the error signals are of the order of a few gigahertz, whereas those of the error signal difference are $1/2$ orders of magnitude lower. We note that error signals do not represent frequency adequately because they may incorporate laser drifts, as well as piezoelectric (such as hysteresis and creep). Indeed, a better choice is to analyze the beat signal directly. This is because the beat frequency can be fully attributed to the MRR frequency separation and decoupled from the laser fluctuations.

Next, following the above discussion, we analyze the beat frequency obtained by tapping about 10% of the signal emerging from each of the two lasers, combining it into a single fiber and detecting the combined signal using a fast photodetector connected to a frequency counter, as illustrated in the left portion of Fig. 3. For this purpose, a wafer scale set of cascaded MRRs has been fabricated by UV lithography, and a specific set of MRRs separated by ~ 4 GHz has been selected. We once again stress that this frequency separation is most likely a consequence of fabrication tolerances. In Fig. 5 we plot the normalized frequency difference ($\Delta f/f$) as a function of time, while switching among three modes of operation of the servo-loops to reveal the different stability characteristics of the system components. In Fig. 5(a) we present the case where, initially (denoted as $t = 0$), each of the two lasers is locked to its dedicated MRR, followed by the mode in which one laser is free running, while the other is still locked, and finally once again both lasers are locked. As can be seen, when the lasers are locked to both MRRs we obtain a relatively constant frequency difference. This is in contrast to the case where one laser is locked to a MRR and the system drifts. Next, in Fig. 5(b) we plot the measured normalized frequency

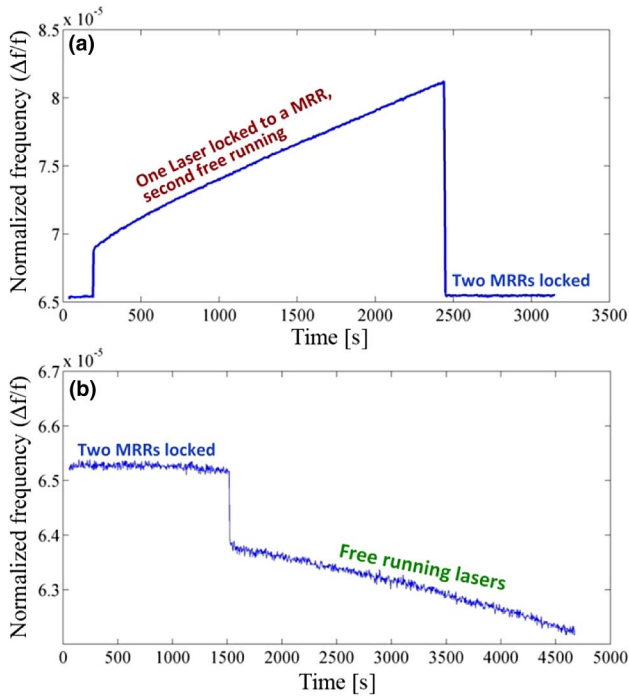


Fig. 5. Normalized frequency difference as a function of time for two different operation regimes: (a) one laser locked to a MRR and the second laser free running, and subsequently both lasers locked to both MRRs, and (b) two lasers locked to both MRRs and subsequently both lasers free running.

difference for the case where initially each of the two lasers is locked to its dedicated MRR, and subsequently both lasers are free running. Once again, the system seems to drift significantly when the lasers are free running, representing the relative instability of the two lasers. The magnitude of this drift is appreciably lower than that of that presented in Fig. 5(a). We conclude that when operating in the case of a single servo-loop, considering the relatively long time constants, we are most likely tracking the MRR drift, which is dominant with respect to the laser drift. Indeed, as the MRR temperature is not stabilized in any manner, such drifts, which correspond to a relative frequency drift of $\sim 10^{-5}$ over the course of ~ 40 min, are highly likely, as they correspond to a temperature drift of ~ 0.1 mK (considering a thermo-optic coefficient of the order of $\sim 10^{-4}/^\circ\text{C}$).

Next, we turn to analyze the instability of the beat frequency representing the frequency difference instabilities between the two MRRs. To comply with the widespread and conventional frequency stability analysis, we apply an overlapping Allan deviation to the measured normalized frequency presented in Fig. 5.

The Allan variance is a highly common time domain measure of frequency stability. Similar to the standard variance, it is a measure of the fractional frequency fluctuations, and yet has the advantage of being convergent for most types of noise. For a discrete series of N measurements, the Allan variance can be defined as follows [32]:

$$\sigma_y^2(\tau) = \frac{1}{2(N-1)} \sum_{k=1}^{N-1} (y_{k+1} - y_k)^2,$$

where y_k is the fractional frequency of sample k , averaged on the time interval τ . Here, we use an overlapping Allan deviation that

is an implementation of the Allan deviation utilizing all possible combinations of the measured dataset.

The normalized frequency is translated to refractive index units by multiplying the normalized frequency by the effective group index of the guided mode. In Fig. 6 we plot the overlapping Allan deviation as a function of integration time τ for three different scenarios. The first, represented in blue, corresponds to the case where each of the lasers is locked to its dedicated MRR. The significance of applying this approach is twofold. First, it quantifies the sensor metrics in the time domain, i.e., it reveals the instability of the sensor at different time constants. Second, the Allan deviation is a very powerful tool to discern different noise sources by examining the slope at different time constants. For instance, as one can see, the instability of the locked system averages out at a rate of $\sim \frac{1}{\sqrt{\tau}}$, revealing our system at these time constants (3–100 s) to be white frequency noise limited [33]. At the time constant of ~ 200 s, the slope levels out, which is typical of frequency flicker noise. The sensor reaches a floor of $\sim 1.5 \cdot 10^{-8}$, representing the ability to measure variations in index of refraction with unprecedented precision approaching 10^{-8} at these time constants. Even if we take into account a realistic biosensing or gas-sensing scenario in which the optical mode interacts with the analyte only partially due to the limited mode confinement in the cladding, we still maintain precision beyond the state of the art.

Next, we compare our result to the free-running case (green line) and the single lock case (red line). Clearly, one can see the trend illustrated in Fig. 5 revealed in this analysis. The single lock, as well as the free-running lasers, exhibit significant instable operation at long times when compared to the double MRR lock scheme. Such plots exemplify the long time stability advantages of our system. A single MRR shows excellent short time stability (~ 3 s) comparable to the two rings. Yet, as laser drifts (green line) and temperature drifts of the MRRs (red line) become dominant, the system loses its ability to precisely measure refractive index changes. We note that even when we remove the relatively deterministic linear drift from our analysis (not shown here), both the free-running lasers and the single MRR lock schemes still exhibit significant instability in comparison with our two-MRR system. We note that although both MRRs are subjected to the same thermal environment, varying temperature gradients across the chip

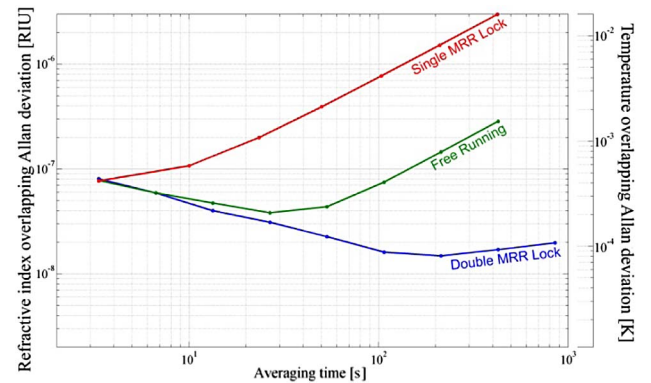


Fig. 6. Overlapping Allan deviation (based on measurements in Fig. 5) of the refractive index presented for three cases: a single laser locked to an MRR with the second laser free running (red line), two lasers free running (green line), and the case where each of the two lasers is locked to its dedicated MRR (blue line).

(resulting from the absence of thermal management and/or isolation of our chip, in the current demonstration) might induce slight fluctuations and drifts in the fractional frequency. Another mechanism that may induce such drifts is related to imperfections in the servo-loop, e.g., in the form of a parasitic (and drifting) input to the integrator. Indeed, we witness a small frequency drift of the order of 10^{-7} RIU/h. Investigation of the exact mechanism of such small and yet important drifts will be pursued in the future.

Generally, we further note that our laser's linewidth and overall performance affects the servo-loop performance. Indeed, our laser's linewidth is narrower than the linewidth of the ring resonances. In principle, lasers with larger phase noise would require longer integration times in order to achieve the same performance.

C. Chip-Scale Thermometry

When translating the normalized frequency uncertainty of our double-locked MRR system in terms of temperature sensitivity (right axis in Fig. 6), one reveals an unprecedented ability to implement on-chip precise thermometry. Here, a temperature difference precision of $1.2 \text{ mK} \cdot \tau^{-1/2}$ with a floor of $\sim 90 \text{ } \mu\text{K}$ at 200 s is predicted. To demonstrate such capabilities explicitly, we introduce a localized source of light illuminating one of the MRRs [see Fig. 7(a)], and thus by direct absorption create a deliberate temperature gradient. To create such localized illumination, we use a near-field optical microscope (NSOM) in which a fiber coupled probe, with an aperture of 300 nm , is used in illumination mode. The NSOM probe is set to be in contact with the surface, and positioned at the center of one of the MRRs [Fig. 7(a)]. Operating at the wavelength of 980 nm , we expect the light to diffract into the silicon dioxide layer (having a thickness of $2 \text{ } \mu\text{m}$), and then be absorbed at the silicon substrate beneath it. Such a process generates a lateral heat gradient across the chip, which can be measured precisely using our cascaded double-locked MRR apparatus. In Fig. 7(b) we plot the temperature difference (calculated using the relation $\Delta T = n_g \Delta f / (f \alpha)$, where α is the thermo-optic coefficient of silicon and n_g is the effective group index of refraction) between the two MRRs as a function of time. The temperature gradient is controlled by varying the power coupled to the NSOM probe. To maintain a reference baseline, we turn off the laser in between each illumination sequence, and compensate for a small linear drift. As we decrease the power level, we also intentionally increase the time we measure the temperature difference in order to obtain a better signal-to-noise level.

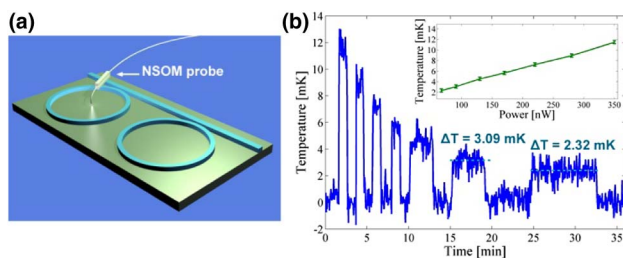


Fig. 7. (a) Schematic illustration of our NSOM tip illuminating light on the left MRR, and thus creating a heat gradient via optical absorption in the silicon bottom layer. (b) Temperature difference between the two MRRs as inferred from the measured beat frequency as a function of time, while changing the optical power illuminated by the NSOM probe. Inset: temperature as a function of illuminating power.

As can be seen in Fig. 7(b) (inset), we apply optical power in the range of a few hundreds of nanowatts (calibrated separately using a photodetector) and obtain a linear temperature offset of a few millikelvin. For the last illumination sequences in the Fig. 7(b) (corresponding to power levels of ~ 90 and $\sim 70 \text{ nW}$; see dashed horizontal lines) we measure corresponding average temperatures of 3.09 mK and 2.32 mK , i.e., a difference of $800 \text{ } \mu\text{K}$ between the two measurements. From the Allan deviation curve we estimate the uncertainty to be of $\sim 90 \text{ } \mu\text{K}$ at the measurements time constant ($\sim 300 \text{ s}$). It is thus not surprising that we can easily differentiate between these two temperatures.

In recent years, there has been significant effort to construct optical chip-scale thermometers, with designs exploiting both photonic crystal cavities and MRRs. Such devices offer prominent advantages with respect to other temperature measurement techniques, as they offer high sensitivity, large temperature range, and immunity to electro-magnetic disturbance. The cascaded double-locking scheme presented here not only compares favorably in its sensitivity, but also allows one to keep this high degree of precision over long times, without the need to stabilize both the chip and the interrogating system. As such, our approach offers fantastic prospects in terms of integration with relatively cheap and compact lasers, such vertical-cavity surface-emitting lasers (VCSELs).

3. DISCUSSION

We have demonstrated an on-chip sensor capable of detecting unprecedentedly small frequency changes, which can be traced back to minute perturbations in refractive index or temperature. Our approach consists of two cascaded microring resonators; one serves as the sensing device, while the other plays the role of a reference, eliminating environmental and system fluctuations (temperature, laser frequency, etc.). By utilizing a servo-loop locking scheme, we are able to translate the measured effects from the optical domain to the radio frequency domain. By doing so, we can quantify our system capabilities utilizing the well-established RF technologies, such as frequency counters, spectrum analyzers, and atomic standards.

Experimentally, we have locked two lasers to the two cascaded MRRs such that each of the lasers is now aligned to its respective MRR. By tracking the error signals of the servo-loops we note that, while each error signal drifts significantly (\sim few gigahertz), the difference in error drifts about 2 orders of magnitude less ($\sim 50 \text{ MHz}$). Generally, error signals cannot be directly mapped to frequency deviations (due to laser frequency drift, laser piezo hysteresis, etc.). Yet this result exemplifies the advantage of using a reference resonator to address environmental perturbations.

To fully exploit the system capabilities to convert optical frequencies to the RF domain, we directly measured the beat frequency between the two lasers. First, by directly observing frequency over time we observed that the laser drift is significantly smaller than the drifts of the MRRs in an uncontrolled environment. Hence, MRRs are shown to be unstable frequency references over long times, and thus the sensing capabilities are limited. In contrast, by analyzing the beat signal of the locked lasers, we could observe stable frequency, up to the level of $\sim 10 \text{ MHz/h}$. Utilizing the well-established techniques borrowed from the disciplines of frequency metrology, we calculate the Allan deviation and find our system to be capable of observing extremely low perturbations in refractive index, down to the level

of $7 \cdot 10^{-9}$ at 200 s. The abovementioned value can be used for the purpose of temperature sensing down to the 50 μK level. Indeed, by taking advantage of the interband transition, we used a near-field light probe as a local heat source and we explicitly demonstrate the usefulness of our approach for temperature-sensing applications. We could easily observe temperature difference of 500 μK with high signal-to-noise ratio.

While having an on-chip thermometer with 50 μK temperature precision is, to the best of our knowledge, the state of the art in the field, it is tempting to consider further advancements. The precision scales with the Q -factor and the signal-to-noise ratio. As we have recently reported, silicon MRRs with Q -factors of $\sim 5 \cdot 10^6$ can be achieved [23]. Thus, assuming the same signal-to-noise ratio as in our current demonstration, one may expect temperature sensing precision below 1 μK and refractive index sensing in the 10^{-10} regime. Obviously, achieving such fantastic results should require additional system efforts such as thermal management, and mechanical stability. An additional important consideration for implementing a temperature sensor, in contrast to a refractive index sensor, is the need to separate spatially the temperature sensing MRR from the reference MRR. For instance, to probe the variation in temperature across the chip, one would ideally deploy several MRRs in different locations across the chip. Another important issue is the ability to fully calibrate such sensors. Indeed, introducing a highly calibrated refractive index change is highly challenging to achieve, as a fully traceable refractive index standard does not exist. The major challenge to our obtaining a fully traceable sensor will probably be a topic of interest in the years to come.

Next, we discuss our system from the engineering perspective of implementing the above-demonstrated platform as a refractive index sensor. For implementing a refractive index sensor and maintaining the same principle of operation mentioned above, one would like both MRRs to be subjected to the same cladding environment (discarding the sensing analytes). One approach, recently demonstrated by Kim *et al.*, is to construct a liquid-based refractive index sensor having a common flow cell above both MRRs that is able to maintain the flow of two solutions above each MRR separately [15]. A second approach is to construct a gas-based sensor, where both MRRs have hollow chambers above them. Here, the reference MRR is encapsulated and the sensing MRR is exposed to the environment. Similar designs have been reported in the context of atomic spectroscopy with rubidium atoms integrated above a MRR [34]. Finally, we address the prospects of fully integrating the above-demonstrated system, including sources, detectors, and servo-loops, into a chip-scale sensor. To do so, we propose to exploit the fantastic achievements in miniaturized components such as vertical-cavity surface-emitting lasers (VCSELs), microprocessors, and voltage-controlled oscillators. Inspired by the revolution in chip-scale atomic clocks [35], sharing similar frequency-locked loop architectures, we believe that a fully integrated low-cost and low power consuming frequency-locked cascaded sensing system is feasible.

Funding. European Research Council (ERC) (ERC-LIVIN 648575).

Acknowledgment. The authors thank Mr. Yoel Sebbag for fruitful discussions. The MRRs were fabricated at the Center for Nanoscience and Nanotechnology, The Hebrew University of Jerusalem.

REFERENCES

1. J. N. Anker, W. P. Hall, O. Lyandres, N. C. Shah, J. Zhao, and R. P. Van Duyne, "Biosensing with plasmonic nanosensors," *Nat. Mater.* **7**, 442–453 (2008).
2. A. F. Gavela, D. G. García, J. C. Ramirez, and L. M. Lechuga, "Last advances in silicon-based optical biosensors," *Sensors* **16**, 285–300 (2016).
3. V. Venkataraman, K. Saha, and A. L. Gaeta, "Phase modulation at the few-photon level for weak-nonlinearity-based quantum computing," *Nat. Photonics* **7**, 138–141 (2012).
4. M. Mesch, B. Metzger, M. Hentschel, and H. Giessen, "Nonlinear plasmonic sensing," *Nano Lett.* **16**, 3155–3159 (2016).
5. A. B. Evlyukhin, S. I. Bozhevolnyi, A. Pors, M. G. Nielsen, I. P. Radko, M. Willatzen, and O. Albrechtsen, "Detuned electrical dipoles for plasmonic sensing," *Nano Lett.* **10**, 4571–4577 (2010).
6. J. T. Robinson, L. Chen, and M. Lipson, "On-chip gas detection in silicon optical microcavities," *Opt. Express* **16**, 4296–4301 (2008).
7. H. Xu, M. Hafezi, J. Fan, J. M. Taylor, G. F. Strouse, and Z. Ahmed, "Ultra-sensitive chip-based photonic temperature sensor using ring resonator structures," *Opt. Express* **22**, 3098–3104 (2014).
8. P. F. Egan, J. A. Stone, J. H. Hendricks, J. E. Ricker, G. E. Scace, and G. F. Strouse, "Performance of a dual Fabry–Perot cavity refractometer," *Opt. Lett.* **40**, 3945–3948 (2015).
9. S. Poeggel, D. Tosi, D. Duraibabu, G. Leen, D. McGrath, and E. Lewis, "Optical fibre pressure sensors in medical applications," *Sensors* **15**, 17115–17148 (2015).
10. X. Zhao, J. M. Tsai, H. Cai, X. M. Ji, J. Zhou, M. H. Bao, Y. P. Huang, D. L. Kwong, and A. Q. Liu, "A nano-opto-mechanical pressure sensor via ring resonator," *Opt. Express* **20**, 8535–8542 (2012).
11. A. C. Liapis, B. Gao, M. R. Siddiqui, Z. Shi, and R. W. Boyd, "On-chip spectroscopy with thermally tuned high-Q photonic crystal cavities," *Appl. Phys. Lett.* **108**, 021105 (2016).
12. K. De Vos, I. Bartolozzi, E. Schacht, P. Bienstman, and R. Baets, "Silicon-on-Insulator microring resonator for sensitive and label-free biosensing," *Opt. Express* **15**, 7610–7615 (2007).
13. S. M. Grist, S. A. Schmidt, J. Flueckiger, V. Donzella, W. Shi, S. Talebi Fard, J. T. Kirk, D. M. Ratner, K. C. Cheung, and L. Chrostowski, "Silicon photonic micro-disk resonators for label-free biosensing," *Opt. Express* **21**, 7994–8006 (2013).
14. T. Claes, W. Bogaerts, and P. Bienstman, "Experimental characterization of a silicon photonic biosensor consisting of two cascaded ring resonators based on the Vernier-effect and introduction of a curve fitting method for an improved detection limit," *Opt. Express* **18**, 22747–22761 (2010).
15. D. Kim, P. Popescu, M. Harfouche, J. Sendowski, M.-E. Dimitsantou, R. C. Flagan, and A. Yariv, "On-chip integrated differential optical microring refractive index sensing platform based on a laminar flow scheme," *Opt. Lett.* **40**, 4106–4109 (2015).
16. G. C. Bjorklund, M. D. Levenson, W. Lenth, and C. Ortiz, "Frequency modulation (FM) spectroscopy," *Appl. Phys. B* **32**, 145–152 (1983).
17. R. W. P. Drever, J. L. Hall, F. V. Kowalski, J. Hough, G. M. Ford, A. J. Munley, and H. Ward, "Laser phase and frequency stabilization using an optical resonator," *Appl. Phys. B* **31**, 97–105 (1983).
18. D. S. Bomse, A. C. Stanton, and J. A. Silver, "Frequency modulation and wavelength modulation spectroscopies: comparison of experimental methods using a lead-salt diode laser," *Appl. Opt.* **31**, 718–731 (1992).
19. T. Carmon, T. J. Kippenberg, L. Yang, H. Rokhsari, S. Spillane, and K. J. Vahala, "Feedback control of ultra-high-Q microcavities: application to micro-Raman lasers and microparametric oscillators," *Opt. Express* **13**, 3558–3566 (2005).
20. P. Del'Haye, O. Arcizet, A. Schliesser, R. Holzwarth, and T. J. Kippenberg, "Full stabilization of a microresonator-based optical frequency comb," *Phys. Rev. Lett.* **101**, 053903 (2008).
21. L. Stern, I. Goykhman, B. Desiatov, and U. Levy, "Frequency locked micro disk resonator for real time and precise monitoring of refractive index," *Opt. Lett.* **37**, 1313–1315 (2012).
22. J. Vanier, "Atomic clocks based on coherent population trapping: a review," *Appl. Phys. B* **81**, 421–442 (2005).
23. A. Naiman, B. Desiatov, L. Stern, N. Mazurski, J. Shappir, and U. Levy, "Ultrahigh-Q silicon resonators in a planarized local oxidation of silicon platform," *Opt. Lett.* **40**, 1892–1895 (2015).

24. B. Desiatov, I. Goykhman, and U. Levy, "Demonstration of submicron square-like silicon waveguide using optimized LOCOS process," *Opt. Express* **18**, 18592–18597 (2010).
25. J. Cardenas, C. B. Poitras, J. T. Robinson, K. Preston, L. Chen, and M. Lipson, "Low loss etchless silicon photonic waveguides," *Opt. Express* **17**, 4752–4757 (2009).
26. M. P. Nezhad, O. Bondarenko, M. Khajavikhan, A. Simic, and Y. Fainman, "Etch-free low loss silicon waveguides using hydrogen silsesquioxane oxidation masks," *Opt. Express* **19**, 18827–18832 (2011).
27. J. Vanier and C. Audoin, *The Quantum Physics of Atomic Frequency Standards* (Hilger, 1989).
28. M. S. Taubman and J. L. Hall, "Cancellation of laser dither modulation from optical frequency standards," *Opt. Lett.* **25**, 311–313 (2000).
29. F. Träger, *Springer Handbook of Lasers and Optics* (Springer, 2012).
30. J. L. Hall and M. S. Taubman, "Laser stabilization," in *Handbook of Optics*, 2nd ed. (2001).
31. J. Komma, C. Schwarz, G. Hofmann, D. Heinert, and R. Nawrodt, "Thermo-optic coefficient of silicon at 1550 nm and cryogenic temperatures," *Appl. Phys. Lett.* **101**, 041905 (2012).
32. D. W. Allan, "Should the classical variance be used as a basic measure in standards metrology?" *IEEE Trans. Instrum. Meas.* **IM-36**, 646–654 (1987).
33. J. Levine, "Introduction to time and frequency metrology," *Rev. Sci. Instrum.* **70**, 2567 (1999).
34. L. Stern, R. Zektzer, N. Mazurski, and U. Levy, "Enhanced light-vapor interactions and all optical switching in a chip scale micro-ring resonator coupled with atomic vapor," *Laser Photon. Rev.* **10**, 1016–1022 (2016).
35. S. Knappe, V. Shah, P. D. D. Schwindt, L. Hollberg, J. Kitching, L.-A. Liew, and J. Moreland, "A microfabricated atomic clock," *Appl. Phys. Lett.* **85**, 1460–1462 (2004).